RSC Advances

PAPER

View Article Online
View Journal | View Issue

Cite this: *RSC Adv.*, 2026, **16**, 15020

Assessment of the efficacy of agarose and agarose augmented with zinc oxide, carbon dots, and graphitic carbon nitride nanostructures in the restoration of historic tintype

Hadeer M. ElDeeb, *[a] Mona F. Ali, [a] Maha A. Ali, [a] Nasser N. Morgan[b] and Ahmed N. Emam *[cd]

Tintype photographs, a popular medium in the 19th century, provide valuable cultural and historical records. However, they are frequently at risk due to surface contaminants, such as soot and dust, which compromise both the visual appearance and the chemical stability of tintypes. The sheet-like nature of tintypes makes them highly susceptible to damage from conventional cleaning methods, which can cause scratching and result in partial loss of the image layer. The present work evaluated efficiency of various cleaning techniques, including swab cleaning, agarose gel, and nanomaterial-modified agarose gels incorporating zinc oxide (ZnO), carbon dots (CDots), and graphitic carbon nitride (g-C_3N_4). The nanomaterials and composite gels were characterized in detail using transmission electron microscopy (TEM), dynamic light scattering (DLS), zeta potential, UV-vis spectroscopy, and attenuated total reflectance-Fourier transform infrared (ATR-FTIR) spectroscopy. Cleaning efficiency was also assessed through portable digital microscopy, colorimetric analysis, and ATR-FTIR spectroscopy, prior to and post cleaning as well as after artificial light ageing. The results demonstrated that nanomaterial-functionalized agarose gels offered superior cleaning efficiency and a protective effect in comparison to conventional methods. Interestingly, agarose with ZnO ($\Delta E = 3.35$), carbon dots ($\Delta E = 2.7$), and graphitic carbon nitride ($\Delta E = 3.09$) efficiently removed dust without inducing noticeable color changes while simultaneously providing an additional barrier against UV radiation. Here, ΔE represents the total color difference calculated according to the CIELAB color space and is a dimensionless parameter. In soot removal, agarose + ZnO ($\Delta E = 5.84$) and agarose + carbon dots ($\Delta E = 7.73$) exhibited maximum performance. Significantly, ATR-FTIR analysis confirmed that no chemical alteration in the tintype layers following treatment or accelerated invasive cleaning of tintypes, confirming the suitability of the methods for use in restoration and conservation.

Received 7th January 2026
Accepted 4th March 2026

DOI: 10.1039/d6ra00164e

rsc.li/rsc-advances

1. Introduction

Photographs such as those found in museums, warehouses, and archives are very important and carry artistic, aesthetic, civilizational, historical, and cultural values.[1,2] Through photographic images, different lifestyles are recorded, and the circumstances and style of the artist are reflected.[3] Therefore, it is crucial to safeguard photographs against potential damage. Although interest in maintaining photographs was minimal, attention to this field has increased in the last thirty years.[4] Tintype photography, also known as ferrotype or melainotype photography, emerged in the mid-1850s. It was invented by Adolphe Alexander Martin in France and later patented by Hamilton Smith in the United States.[5,6] Tintypes were created by applying a collodion emulsion to a thin iron sheet coated with a dark lacquer or enamel. Tintypes are multilayer composite structures. The first layer is the metal support plate, which is japanned on one side; this coloured japanning layer provides the dark background for the final image. The second layer is the emulsion, consisting of a collodion binder (*i.e.*, nitrocellulose in ether) and the final image material (*i.e.*, metallic silver). Finally, the third layer is the protective top varnish (Fig. 1).[7,8] Tintype photographs are prone to damage and degradation by several factors, most notably environmental factors. In particular, increased relative humidity promotes corrosion of the metal

[a]*Conservation Department, Faculty of Archaeology, Cairo University, Giza, Egypt. E-mail: hadeermamdouh010@gmail.com; hadeermamdouh010@cu.edu.eg*

[b]*Physics Department, Faculty of Science, Al-Azhar University, Cairo 11884, Egypt*

[c]*Refractories, Ceramics and Building Materials Department, Advanced Materials Technology & Mineral Resources Research Institute, National Research Centre (NRC), El Bohouth St., Dokki, 12622 Cairo, Egypt. E-mail: ahmed.gsc.ndp@gmail.com; an.emam@nrc.sci.eg*

[d]*Nanomedicine & Tissue Engineering Research Lab, Medical Research Centre of Excellence, National Research Centre (NRC), El Bohouth St., Dokki, 12622 Cairo, Egypt*

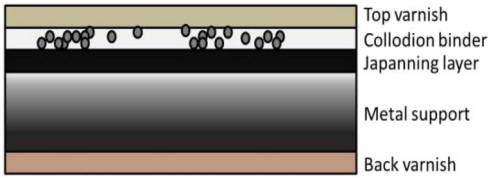

Fig. 1 Structure of tintype photographs. Adapted with a copyright permission from "Rogge, C. E., & Lough, Fluorescence fails: analysis of UVA-induced visible fluorescence and false-color reflected UVA images of tintype varnishes do not discriminate between varnish materials. *Journal of the American Institute for Conservation,* **55**(2), 138–147.

support, primarily through reaction with oxygen, leading to rust formation and delamination.[9,10] Elevated temperatures accelerate the oxidation and chemical degradation of organic components such as collodion and protective varnish, ultimately causing loss of image density and details.[11,12] Additionally, inadequate protection during storage is a major factor that accelerates deterioration. Storing photographs in chemically active enclosures or exposing them to direct light can cause layer discoloration and the appearance of dark or white spots through photochemical reactions.[13] Poor handling practices, such as direct hand contact or dry cleaning, can scratch the photographic surface or damage its delicate layers. Biologically, microbial and fungal activity are secondary processes that can cause image degradation, especially under conditions of low ventilation and high humidity, where fungi, which are organic matter feeders, might grow.[14–16] Tintype photographs use a sensitive photographic medium that is highly susceptible to significant deterioration caused by particulate contaminants such as soot and dust. This vulnerability is due to their physical nature: a thin photographic layer of collodion covered with an organic varnish, bonded to a coated iron support.[17] Fine dust causes heterogeneous particles to deposit on the surface, obscuring visual details and reducing image contrast. Unsuitable removal efforts can result in mechanical abrasion, damage to the varnish layer, or collodion shedding.[18] Soot originates from various combustion sources, such as candles, ordinary heating, or storage environments.[19] It is composed of a sticky carbonaceous material that strongly adheres to the image surface, particularly in the presence of moisture, making its removal extremely difficult without causing permanent damage to the photographic layer.[20] Chemically, some components of dust, *i.e.*, sulphates or nitrates, may catalyse electrochemical corrosion reactions on the iron substrate and lead to rust spots, especially when moisture is present. Soot also contains semi-volatile organic compounds that may react with the varnish or collodion components and lead to yellowing or deterioration of the organic layers.[21]

These are some of the main causes that diminish the documentary and aesthetic value of tintype photographs. These issues also make it difficult to study and restore such photographs, so careful preservation methods are needed that are compatible with both the type of contaminant and the image materials. Standard cleaning methods, such as rubbing with a dry hand or application of general solvents, are not suitable for treating tintype photographs due to their extreme sensitivity and multi-layered nature.[22] Direct handling with inappropriate cloths or brushes may harm the surface of the varnish or collodion, leading to partial or total loss of the image.[23] The application of household chemicals, such as alcohol or domestic cleaning liquids, also leads to the dissolution or softening of organic layers, resulting in colour changes, visual degradation and progressive deterioration.[24] In addition to this, wet cleaning or steam cleaning methods are among the most harmful procedures, as they result in distortion (*e.g.*, bending or undulations) of the metal substrate and increase the likelihood of corrosion or rusting through entrapped moisture.[25] These conditions also favour the development of microscopic fungi, especially if drying is not sufficient. These methods also lack precise control over the extent of contact with the image surface, making them restoratively unsafe and posing a risk to the original optical and physical properties of the image. This directly jeopardizes the integrity of historically valuable photographic artefacts such as tintype photographs.

Agarose gel, a naturally occurring polysaccharide derived from red marine algae, forms a three-dimensional porous network that melts and solidifies reversibly when an aqueous solution is heated and then cooled. The structure, composed of repeating units of disaccharides galactose and anhydrogalactose, is responsible for the novel properties of the gel. The pore size in the gel can be accurately controlled by varying the agarose concentration.[26] Agarose gel is of considerable use in photographic conservation due to its controlled release system.[27] It permits controlled and localized use of aqueous solvents and solutions that minimize, to a large extent, overwetting that leads to degradation of the metal substrate, distortion or fungal growth. Its chemical inertness also prevents secondary reactions with photographic materials.[28] Agarose gel further reduces abrasive mechanical cleaning by softening stains and dirt for easy removal. This controlled technique guarantees that the natural optical and physical characteristics of vintage photographic objects, such as tintypes, remain as originally conceived, and it is thus a valuable resource for preserving their long-term integrity.[12]

Carbon dots (CDots), zero-dimensional carbon nanomaterials, are emerging as a highly versatile tool for a wide variety of applications, including UV protection. Since their accidental discovery in 2004,[29] CDots have rapidly grown to become an area of interest due to their inherent UV absorption characteristics, excellent photostability, low cost, simple preparation protocols, and non-toxicity, and because of the abundance of their raw materials. In addition to UV protection, CDots have found broader uses in diverse applications.[30] Owing to their unique properties, significant advances in photocatalysis, LEDs, anti-counterfeit technology, and imaging have been achieved. As awareness of these advantages grows, CDots are expected to play an increasingly important role in the development of next-generation UV-protective materials and devices.

Zinc oxide (ZnO) is an invaluable asset in conservation science because of its multidimensional nature.[31] Its most

prominent use is in protection against UV radiation, where its superior ability to absorb UV rays,[32] particularly in nanoparticle form, protects light-sensitive cultural artefacts such as textiles, paper, and photographs from photodegradation.[33] In addition, ZnO has strong antimicrobial and antifungal properties, which help fight against biodeterioration.[34] Although its photocatalytic activity has promise in self-cleaning systems, its application to organic artwork demands careful control to avoid deterioration.[35] ZnO, historically under the guise of zinc white, is a ubiquitous pigment in works of art, which means conservators must be aware of how it degrades.[36] This research aimed to achieve long-term stability, non-toxicity, and optimum application methods for ZnO to enable its safe use in benefiting cultural heritage conservation.

Graphitic carbon nitride (g-C_3N_4), a metal-free organic semiconductor, offers excellent advantages for the conservation of organic cultural heritage materials. It is an extremely promising material for protective coatings owing to its strong UV absorption and excellent photostability, which can shelter sensitive artifacts from destructive light-induced degradation.[37] Furthermore, g-C_3N_4 has antimicrobial and antifungal properties that offer significant protection against biodeterioration.[38] While its photocatalytic activity may be exploited for controlled contaminant removal, careful research needs to be undertaken to determine its non-degrading application to sensitive organic substrates. g-C_3N_4 is also notable for its chemical and thermal stability, low cost, and environmentally benign nature.

The current study aimed to evaluate the efficiency of traditional and newly developed methods, namely, traditional swab cleaning, agarose gel, and agarose gel enhanced with nanomaterials (*i.e.*, zinc oxide, carbon dots, and graphitic carbon nitride), in removing soot deposits and particulate dust from the surfaces of tintype photographs. In addition, the study investigates the role of these materials in protecting the image surface against UV-induced damage. The evaluation was carried out using a portable digital microscope, colorimetric measurements, and attenuated total reflectance-Fourier transform infrared ATR-FTIR) spectroscopy.

2. Experimental

2.1. Materials

Citric acid monohydrate (CA, $C_6H_8O_7 \cdot H_2O$, 99.0%) was purchased from LOBA Chemie. Ethylenediamine (EDA, NH_2-$CH_2CH_2NH_2$, 99.0%) was purchased from Alpha Chemika. Zinc acetate dihydrate (Zn $(CH_3COO)_2 \cdot 2H_2O$, 99.99%) was purchased from Shar Lab S.L. Chemicals, Spain. Sodium carbonate (Na_2CO_3, 98%), and urea (CH_4N_2O, 85%) were purchased from El-Gomhouria Chemicals, Egypt.

2.2. Preparation of carbon dots

Carbon dots (CDots) were prepared *via* the microwave irradiation method previously reported by He *et al.* and Emam and co-workers.[39,40] In brief, about 1.2 g of citric acid (CA, 0.19 M) and 1.58 mL of ethylenediamine (EDA, 0.87 M) were ultrasonically dissolved in 30 mL of distilled water for 10 min, yielding a clear, light-yellow solution. The mixture was then transferred into a 1000 W microwave oven (Fresh) operating at 2450 MHz. The reaction was carried out at a power of 600 W for 13 minutes, producing a dark brown crude product at the bottom of the vessels. The resulting material was dissolved in 100 mL of distilled water and used for further characterization.

2.3. Preparation of zinc oxide nanoparticles

ZnO nanoparticles were synthesized *via* the co-precipitation method with slight changes, adhering to previously established protocols.[41,42] An aqueous solution of zinc acetate dihydrate (0.1 M, 200 mL) was placed in the reaction vessel and heated at 80 °C under vigorous stirring. Subsequently, 200 mL of 0.1 M sodium carbonate solution was added dropwise to the reaction vessel while maintaining the temperature at 80 °C and continuous stirring to ensure optimal particle formation kinetics. A milky suspension was formed at the end of the reaction, indicating the formation of $Zn(OH)_2$ nanoparticles. The resulting white precipitate was purified by centrifugation. After overnight drying at 100 °C, the purified solid was heated at 300 °C for four hours under ambient air, yielding the final ZnO nanoparticles.[43,44]

2.4. Preparation of exfoliated graphitic carbon nitride

Graphitic carbon nitride (g-C_3N_4) was synthesized by thermal decomposition, following previously reported procedures.[44–47] Pristine g-C_3N_4 was prepared by heating urea in a muffle furnace in air. A measured amount of urea was placed in a porcelain crucible, heated to 550 °C at 10 °C min^{-1}, and held at 550 °C for 2 h. Under these conditions, urea undergoes thermal condensation to polymeric g-C_3N_4 rather than complete oxidation to gaseous products, as reported in previous studies. After cooling naturally to room temperature, the obtained g-C_3N_4 was collected and ground into a fine powder. To obtain g-C_3N_4 nanosheets, the as-prepared bulk g-C_3N_4 was again thermally treated using the above heating protocol, but heated for 1 h to induce further thermal exfoliation of stacked bulk g-C_3N_4 into nanosheets.

2.5. Preparation of aged-stained samples

The specimen is a tintype photograph dating back to the nineteenth century and represents one of the images from a private collection owned by Dr Francis A_{min}. The image was segmented into tiny squares with a stencil, roughly 13 squares for the image. For the artificial soiling, dust was prepared by blending clay powder with a small amount of distilled water and mixing the suspension thoroughly with a brush. Soot was collected from a gas lamp onto a glass plate; the resulting powder was transferred to a glass beaker, moistened with a small amount of distilled water, and supplemented with a drop of gum Arabic before being thoroughly mixed with a brush. Both dust and soot were applied with a brush to the designated sections of the photographic image. Subsequently, the samples were aged by placing them in an oven at 60 °C for 3 hours until the applied dirt layers were completely dry. Fig. 2 illustrates the sample preparation procedure. The method for

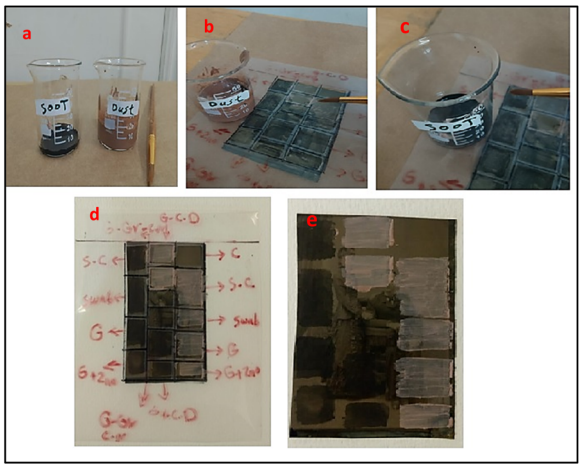

Fig. 2 Steps used to prepare the test photograph: (a) dust and soot, (b) application of dust, (c) application of soot, (d) division of the photo, and (e) after application of the dust and soot contamination.

applying dust and soot to the tintype photographs followed the reported protocol by Hassan and co-workers.[21]

2.6. Preparation of agarose gel and agarose gel with the nanomaterials

Agarose-based gel systems were selected for this research due to their proven effectiveness in cleaning manuscripts and various artistic and historical materials. In this study, the agarose gel was prepared at a concentration of 2% in distilled water. A weighed quantity of agarose powder from Viviants Technologies Sdn Bhd (molecular biology grade U.S.A.) was added to a glass beaker containing 100 mL of distilled water, and the mixture was heated on an electric heater until fully dissolved. Once prepared, the agarose-based gel was poured into a Petri dish to form a layer approximately 0.3 mm thick.[27] Regarding the incorporated nanomaterials, three varieties were utilized due to their effectiveness in self-cleaning and ultraviolet protection: zinc oxide, carbon dots, and graphite carbon nitride. Each nanomaterial (0.5 g) was weighed and placed into separate glass beakers for preparation. In parallel, 2 g of agarose was measured and combined with 100 mL of distilled water, followed by sonication to ensure complete dissolution. The mixtures were then heated on an electric heater at 85 °C until they reached a thick, homogeneous consistency. Each mixture was subsequently poured into Petri dishes to form layers approximately 0.5 cm thick.

2.7. Characterization

Optical properties such as UV-vis absorption spectra for the as-prepared C-dots, ZnO and g-C_3N_4 nanostructures before and after embedding in agarose films were recorded using TG-80 PG instruments, England, within the range 200–900 nm, with a step size of 5 nm. The morphological properties were investigated using transmission electron microscopy (TEM) (JEM-2100F, JEOL, Japan), working at 160 kV.

In addition, the colloidal properties, including particle size distribution and zeta potential, were measured using a Malvern Zeta-sizer Nano ZS instrument. The measurements employed backscatter optics with a He/Ne laser (633 nm) at a 173° scattering angle.

FT-IR spectroscopy was employed to identify the functional groups present in the as-prepared pristine nanostructures as well as in the nanostructures embedded within agarose films, to investigate potential interactions between the agarose and CDots, ZnO, and g-C_3N_4. ATR-FTIR absorbance spectra were recorded over the range of 400–4000 cm^{-1} using a JASCO 6700 Fourier-transform infrared spectrometer (FT-IR).

2.8. Assessment methods

2.8.1. Portable digital microscope. A portable digital microscope was used to examine the surface changes of samples before and after cleaning with agarose gel and gel incorporating nanomaterials, as well as to assess the efficiency of the cleaning process in preserving the surface against UV ageing. A Super Eyes PZ01 500X USB digital microscope (Faculty of Archaeology, Cairo University) was used.

2.8.2. Colorimetric measurements. Colorimetric measurements were performed to evaluate the changes in color of the tintype photographs. Measurements were performed before and after cleaning, as well as after UV ageing, using an Optimatch 3100® spectrophotometer from the SDL Company. All samples were measured in the visible region, *i.e.*, a wavelength range from 400 to 700 nm, with an interval of 10 nm using a D65 light source and an observed angle of 10°. The CIELAB colour parameters (L^* a^* b^*) were used to express colour change. These data were used to calculate the total color difference parameter ΔE^*. When a colour is expressed in CIELAB ($L^*a^*b^*$), L^* defines lightness and varies from 0 (black) to 100 (white), a^* denotes red/green value, where $+a$ means red and $-a$ means green. The b^* scale measures yellow/blue, where $+b^*$ indicates yellow and $-b^*$ indicates blue. The total colour difference ΔE^* can be calculated from the following equation.[16]

$$\Delta E^* = (\Delta L^{*2} + \Delta a^{*2} + \Delta b^{*2})^{1/2}$$

2.8.3. Attenuated total reflectance-Fourier transform infrared (ATR-FTIR) spectroscopy. ATR-FTIR spectroscopy was employed to analyse changes in the chemical structure of the samples after cleaning with both conventional methods (with cotton swabs) and innovative approaches (with agarose gel and gel incorporating nanomaterials). The technique was also used to evaluate the effectiveness of these cleaning methods in protecting tintype images from UV-induced deterioration. IR spectra of the images were recorded using a Bruker Vertex 70 instrument in attenuated total reflection (ATR) mode with a zinc selenide crystal, at wavelengths ranging from 400 to 4000 cm^{-1}. The IR transmittance frequencies of the samples were recorded with an average of 128 scans and a spectral resolution of approximately 4 cm^{-1} at the Projects Sector of the Ministry of Antiquities in Cairo, Egypt.

3. Results and discussion

3.1. Optical properties of carbon dots, zinc oxide and graphitic carbon nitride nanostructures embedded into agarose gel

Fig. 3 presents the UV-vis absorption spectral analysis, revealing distinct optical characteristics for pristine carbon dots (CDots), zinc oxide (ZnO NPs), and graphitic carbon nitride (g-C_3N_4) nanostructures. Each has distinctive spectral characteristics reflective of its corresponding electronic structure. The pristine carbon dots (CDots) system is represented by the black curve and is characterized by a narrow, well-resolved peak at 350 nm, characteristic of n → π* electronic transitions of the sp^3 hybridized aromatic carbon core (*i.e.* C=O) framework.[48] An additional peak is observed at 240 nm, corresponding to π–π* transitions of aromatic –C=C– and –C–C– bonds in the sp^2 hybridized domain of the graphitic core.[40,48] This sharp peak profile reflects good size homogeneity and distribution within the agarose matrix, and the minimal absorption at wavelengths above 400 nm suggests the presence of small, well-passivated carbon nanoparticles, with quantum confinement, contributing to their optical properties.[40,48]

The pristine g-C_3N_4 nanostructures, represented by the red curve in Fig. 3, exhibit a more complex spectral behavior, with two absorption peaks at 325 nm and 392 nm, along with extended absorption into the visible region. The peak at the shorter wavelength of 325 nm is assigned to π → π* transitions of the aromatic C–N heterocycles that make up the graphitic carbon nitride backbone, whereas the feature at 392 nm is assigned to n → π* transitions from nitrogen lone pair electrons.[37] The broad absorption tail extending to approximately 500 nm indicates a relatively small bandgap of *ca.* 2.7–2.8 eV, making this system extremely attractive for visible-light harvesting applications. The spectral breadth also shows some degree of structural disorder or defect states in the g-C_3N_4 framework.[49]

The ZnO NPs sample, represented by the blue curve in Fig. 3, has an evident absorption profile with a principal feature at approximately 367 nm, which is blue-shifted from bulk ZnO.[50,51] This absorption edge corresponds to the band-edge transition between oxygen 2p valence and zinc 3d conduction bands. The

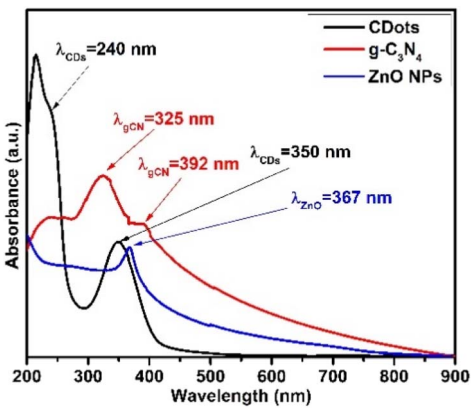

Fig. 3 The UV-vis absorption spectra for the pristine CDots, ZnO NPs and g-C_3N_4 nanostructures.

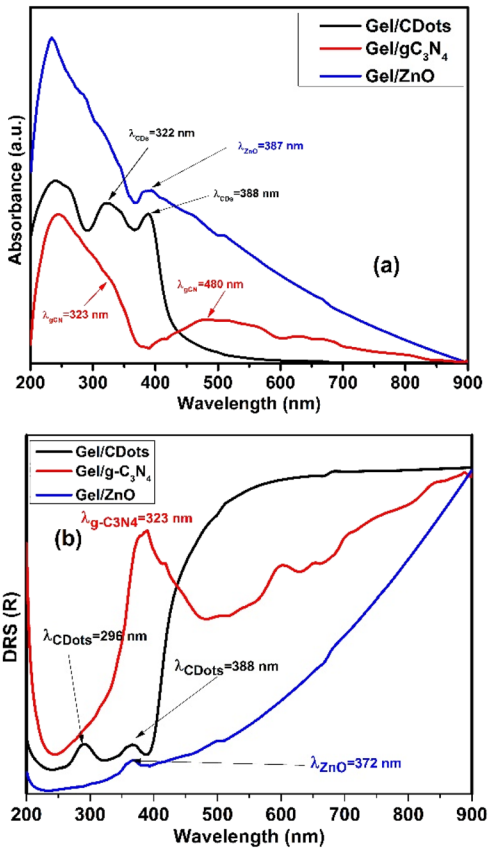

Fig. 4 (a) The UV-vis absorption spectra and (b) diffuse reflectance spectra (DRS) for CDots, ZnO NPs and g-C_3N_4 nanostructures embedded in the agarose gel.

redshift suggests either quantum size effects or the presence of surface defects that affect the electronic band structure.[52,53] The cutoff in absorption near 380 nm confirms the wide bandgap nature of ZnO (approximately 3.3 eV), while the minimal shift shows that the nanoparticles may have special size or morphological properties that influence their optical properties.[54]

Upon the embedding of CDots, ZnO NPs and g-C_3N_4 nanostructures in the agarose films, the absorption spectra exhibited a redshift due to changes in the dielectric constant of the surrounding medium from water to agarose, as shown in Fig. 4a. The gel/ZnO NP composite, represented by the blue line, shows a broad absorption band centered at 387 nm. This feature is associated with well-dispersed ZnO nanoparticles within the gel matrix and with the interaction of ZnO surface states with the polymeric network. The absorption around 387 nm mainly arises from the fundamental band-to-band transition in ZnO, involving electron excitation from the O 2p-dominated valence band to the Zn 4s-dominated conduction band, together with additional contributions from defect-related intra-gap states.[55,56]

The gel/CDots composite, represented by the black line in Fig. 4a, has two main absorption bands at 322 nm and 388 nm, which are related mainly to π–π* transitions in the C=C sp^2 carbon core and n–π* or surface-state transitions associated

with –OH, –COOH, –NH_2, and C=O groups. These results show that the electronic properties of the carbon dots are modified after incorporation into the gel matrix, which is related to interactions with polysaccharide functional groups and results in a balanced UV-vis absorption spectrum.[57,58]

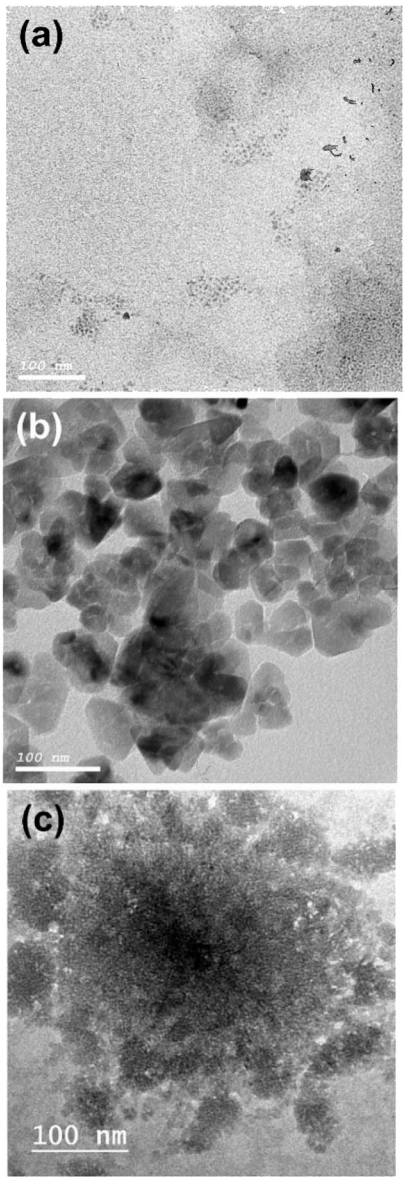

Fig. 5 TEM images for the pristine (a) CDots, (b) ZnO NPs and (c) g-C_3N_4 nanostructures.

Finally, the gel/g-C_3N_4 composite, represented by the red line in Fig. 4a, exhibits two main absorption bands at 333 nm and 480 nm. The band at 480 nm corresponds to the small band gap of g-C_3N_4, which extends absorption into the visible region. This feature arises from the intrinsic π–π* transitions within the conjugated heptazine units and defect-related n–π* transitions associated with the lone-pair electrons on nitrogen atoms. In addition, hydrogen bonding and coordination interactions between the agarose matrix and g-C_3N_4 sheets may slightly alter the local electronic environment, contributing to minor shifts or broadening in the absorption features.[59,60]

These interfacial interactions can (i) modify the local electronic environment and surface states, shifting the band-edge and defect-related transitions, (ii) alter nanoparticle dispersion/aggregation within the gel, and (iii) change the effective refractive index and light-scattering behavior around each nanoparticle domain. These together lead to the observed redshifts, band broadening, and intensity changes in both the UV-vis and DRS spectra upon embedding compared to the pristine colloidal systems.

The diffuse reflectance spectra in Fig. 4b complement these findings and clarify how the embedded nanostructures interact with incident light in the solid-state gel. For gel/CDots, the DRS spectrum exhibits a well-defined minimum (maximum "pseudo-absorption") in the UV region around 296 nm and a second feature around 388 nm, similar to the solution-like absorption features, confirming that the CDots retain their original electronic transitions. For DRS, which involves scattering samples and is normally converted into Kubelka–Munk units to estimate bandgap energy, small shifts in the position of the peaks between absorption and reflectance spectra (*e.g.*, 322 nm *vs.* 296 nm) are expected. These are due to differences in the optical geometry and scattering in the agarose network, rather than changes in the electronic structure.[61–63]

In the case of the gel/g-C_3N_4, there is a well-defined reflectance edge at around 323 nm; after this, there is a gradual decay in reflectance (increase in effective absorption) over the entire range of the visible spectrum. This behavior of the reflectance curve of the compound is like the general behavior of the reflectance curves of g-C_3N_4 materials, in which the absorption edge occurs at around 450 nm but can be affected by the morphology and dispersion of the material in a matrix.[64,65] For gel/ZnO, the DRS spectrum shows a characteristic steep reflectance decrease around 372 nm, corresponding to the fundamental band-gap transition of ZnO, while the reflectance rises steadily at longer wavelengths, confirming that ZnO remains

Table 1 Colloidal properties of the as-prepared CDots, ZnO NPs and g-C_3N_4 nanostructures embedded into the agarose gel

	Dynamic light scattering (DLS)		
Sample	Hydrodynamic diameter (H_D, nm)	Polydispersity index (PDI)	Zeta potential (ξ, mV)
Gel/CDots	33.37 ± 5.145	0.768	−6.62
Gel/ZnO NPs	101.8 ± 21.6	0.985	−3.35
Gel/g-C_3N_4	250.6 ± 40.36	0.905	−5.95

primarily a UV-absorbing component with limited intrinsic visible-light absorption in this configuration.[66,67]

3.2. Morphological and colloidal properties of carbon dots, zinc oxide and graphitic carbon nitride nanostructures

Transmission electron microscopy (TEM) images were used to provide high-resolution morphological analysis of CDots, ZnO NPs and g-C_3N_4 nanostructures, as shown in Fig. 5. Fig. 5a shows the carbon dots (CDots) as small, well-separated spherical nanoparticles with a relatively uniform particle size distribution. The average size distribution was 7.5 ± 2.5 nm, with quasi-spherical morphologies, consistent with previously reported studies.[40] The well-defined spherical morphology and monodisperse distribution signify successful synthesis with excellent control over particle size and shape. The CDots have superior dispersion with minimal or no aggregation and are presented as dark dots on the lighter background.

Fig. 5b shows a TEM image of the ZnO nanoparticles, which displays a distinctly different morphology, consisting of larger, more irregular spherical particles with pronounced agglomeration. The ZnO NPs are seen to form interconnected networks or clusters, with individual particles exhibiting faceted surfaces characteristic of crystalline ZnO. The particles vary in size and shape from nearly spherical to more angular geometries, indicative of a polycrystalline nature.[43,44] The average size distribution is 30 ± 5.5 nm, with quasi-spherical shapes.[54]

Fig. 5c presents a TEM image of the graphitic carbon nitride (g-C_3N_4) material, which exhibits a distinctly different morphology compared with the other two samples. The g-C_3N_4 appears as bulk, sheet-like, or layered structures with rough edges and irregular thickness. These layered morphologies are typical of graphitic materials and reflect the planar arrangement of tri-*s*-triazine units that form the g-C_3N_4 framework, with average lateral dimensions exceeding 100 nm.[68–70]

The colloidal properties of the CDots, ZnO NPs and g-C_3N_4 nanostructures embedded into agarose gel are summarized in Table 1. The gel/CDots composite has the most ideal dispersion properties with the smallest hydrodynamic diameter (33.37 nm), minimum polydispersity index (PDI ∼ 0.768), and most negative zeta potential (−6.62 mV), showing relatively uniform particle distribution and moderate electrostatic stability. The gel/ZnO NPs composite exhibits moderate colloidal properties with an intermediate hydrodynamic diameter (101.8 nm), the highest polydispersity (PDI ∼ 0.985), and the lowest negative zeta potential (−3.35 mV), which indicates moderate particle aggregation and ineffective electrostatic stabilization, reflecting the aggregated morphology shown in the TEM images. The gel/g-C_3N_4 composite shows relatively poor properties, characterized by the largest hydrodynamic diameter (250.6 nm), a high polydispersity index (PDI ≈ 0.905), and a moderately low zeta potential (−5.95 mV). The observed order of colloidal stability (CDots > ZnO > g-C_3N_4) aligns with the morphological observations: the uniform spherical morphology of CDots promotes better dispersion, whereas the crystalline, aggregated ZnO particles exhibit moderate colloidal stability based on their optical and functional performance within the gel matrix.

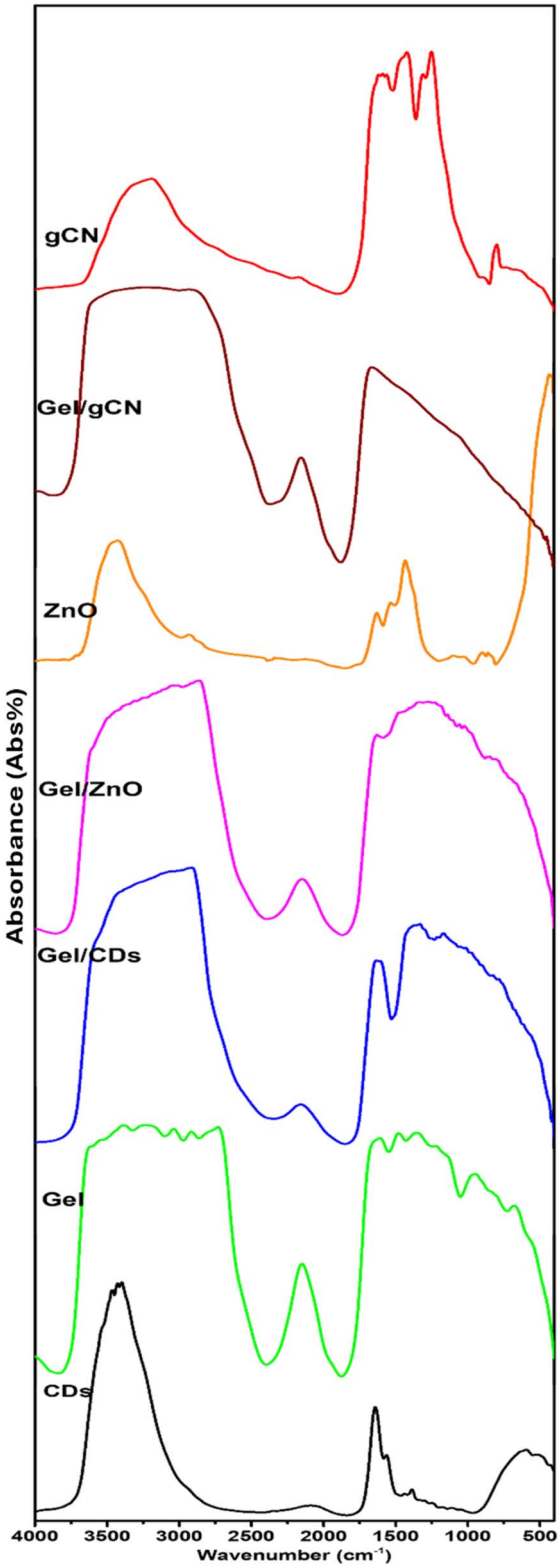

Fig. 6 FT-IR spectra of the pristine CDots, ZnO NPs and g-C_3N_4 nanostructures before and after embedding into the agarose gel.

3.3. Chemical functionalization of the surface of carbon dots, zinc oxide and graphitic carbon nitride nanostructures

Changes in the surface functionalization were investigated *via* ATR/FT-IR spectroscopy, as shown in Fig. 6. The pristine g-C_3N_4 spectrum exhibits characteristic peaks within the 1200–1650 cm^{-1} range, corresponding to the C–N and C=N aromatic stretching vibrations of the heptazine units that form the backbone of the graphitic carbon nitride. The band between 1350 and 1550 cm^{-1} is characteristic of g-C_3N_4, and the band at approximately 810–890 cm^{-1} is assigned to the out-of-plane bending vibration (breathing vibration) of the heptazine ring, a very specific band for the structural motif of the tri-*s*-triazine structure of g-C_3N_4. The broad absorption between 3000–3500 cm^{-1} is indicative of N–H stretching vibrations from terminal amino groups such as $–NH_2$ and –NH, and O–H stretching of adsorbed water molecules, indicating the incompleteness of the condensation reaction and the presence of surface amino groups.[71–73] The FTIR spectrum of the synthesized ZnO nanoparticles exhibits a distinct sharp peak between 400 and 500 cm^{-1}, characteristic of Zn–O lattice stretching vibrations and confirming the formation of ZnO. An additional band at 593 cm^{-1} corresponds to the bending vibrations of Zn–O bonds, reflecting the crystalline nature of ZnO. The observed low-intensity absorption peaks indicate the presence of hydroxyl groups, atmospheric CO_2, and minor organic residues originating from the precursor or synthesis process. A distinct absorption band within the higher frequency around 1400 cm^{-1} corresponds to the stretching vibrations of acetate species (COO^-), confirming residual acetate groups derived from the zinc acetate precursor. In addition, a sharp peak near 1500 cm^{-1} is assigned to the H–O–H bending vibrations, which likely result from trace amounts of adsorbed moisture on the ZnO nanoparticle surface, and confirms the high purity of the synthesized ZnO NPs.[74] Apart from this intense band, a very weak and broad band at 3400 cm^{-1} can be attributed to the O–H stretching vibration of physically adsorbed water molecules on the ZnO surface. Similarly, a small band centered at 1600 cm^{-1} can be related to the H–O–H bending mode of adsorbed moisture. The lack of intense organic bands in the mid-IR region is indicative of the ZnO sample being largely inorganic and devoid of organic residues and stabilizers, which are essential to retain its inherent photocatalytic and antimicrobial activity.[75] The FTIR spectrum of the CDots shows a broad, intense band around 3400–3300 cm^{-1} assigned to overlapping O–H and N–H stretching vibrations, confirming the presence of abundant surface hydroxyl and amino groups that render the dots hydrophilic and reactive. At 2920–2850 cm^{-1}, weak bands correspond to C–H stretching of aliphatic moieties, indicating partial carbonization of the organic precursor into sp^3-hybridized fragments. In the fingerprint region, a prominent band near 1700–1650 cm^{-1} is attributed to C=O stretching of carboxylic/amide groups, while bands around 1570–1500 cm^{-1} and 1450–1400 cm^{-1} arise from C=C/C=N stretching and N–H bending, evidencing a conjugated aromatic or graphitic core decorated with nitrogen-containing functionalities. Below 1300 cm^{-1}, multiple bands between 1250–1000 cm^{-1} are ascribed to C–O–C and C–O stretching of alcohols and ethers, and the features below 900 cm^{-1} correspond to out-of-plane C–H bending of aromatic domains. The results together confirm heteroatom-rich, functionalized carbonaceous nanostructures suitable for interaction with polymeric matrices.[40,76] These are rich functional groups (amino, hydroxyl, carboxyl), characteristic features of carbon dots, that are accountable for their stability and ultra-high biocompatibility.

Upon embedding into agarose gel, pronounced spectral variations are observed for all samples, as shown in Fig. 6. The embedding process is relatively straightforward, relying primarily on electrostatic interactions between the functional groups of the nanomaterials and the available OH groups in agarose.[77] The agarose gel exhibits characteristic peaks at 1000–1200 cm^{-1} (polysaccharide C–O chain stretching), 2900–3000 cm^{-1} (C–H stretch), and a broad O–H stretching band at 3200–3600 cm^{-1}. The embedding process is relatively straightforward, relying primarily on electrostatic interactions between the functional groups of the nanomaterials and the available OH groups in agarose.[77]

In the gel/g-C_3N_4 composite, the triazine bands are preserved but exhibit slight shifts and broadening, indicative of successful integration without structural degradation. In this spectrum, the main g-C_3N_4 bands in the 1650–1200 cm^{-1} range and the heptazine ring signal near 810–890 cm^{-1}, confirm the fundamental conjugated framework of g-C_3N_4. Similarly, the ZnO/gel composite retains the characteristic Zn–O vibrational bands, with additional bands arising from interactions with the polymer matrix. Slight shifts in the amide I and II positions and changes in the band intensities indicate coordination or hydrogen-bond interactions between the carbonyl/amine groups of the gelatin and the Zn^{2+} ions on the ZnO surface, which can enhance interfacial adhesion and dispersion of nanoparticles within the biopolymer. The Zn–O vibration manifests as an intensified absorption in the low-wavenumber region (<600 cm^{-1}), confirming the presence of ZnO within the composite film. The modest modification of the polysaccharidic C–O–C region may arise from altered hydrogen-bonding networks and possible interactions between the ZnO and hydroxyl groups. FTIR analysis confirms strong chemical bonding between ZnO and the agarose matrix, a parameter critical for enhanced performance.[78] The CDots/gel composite has a complex FTIR spectrum, which arises from interactions involving various functional groups. The results show that carbon dots are well incorporated in the agarose gel, as confirmed by the presence of characteristic bands that correspond to carbon dots along with new bands that arise from hydrogen-bonding interactions involving the –OH groups of the gel and the functional groups of the carbon dots.[79] The decreased intensity in the 1800–2300 cm^{-1} region after loading CDots, ZnO and g-C_3N_4 into the gel is consistent with additional hydrogen-bonding and electrostatic interactions between the agarose –OH groups and the surface functional groups of the carbon dots (C=O, C–O, carboxylate, *etc.*), which partially consume or reorganize the free hydroxyl environment and thus attenuate these bands. This spectral change, together with the broader O–H stretching envelope, supports the formation of

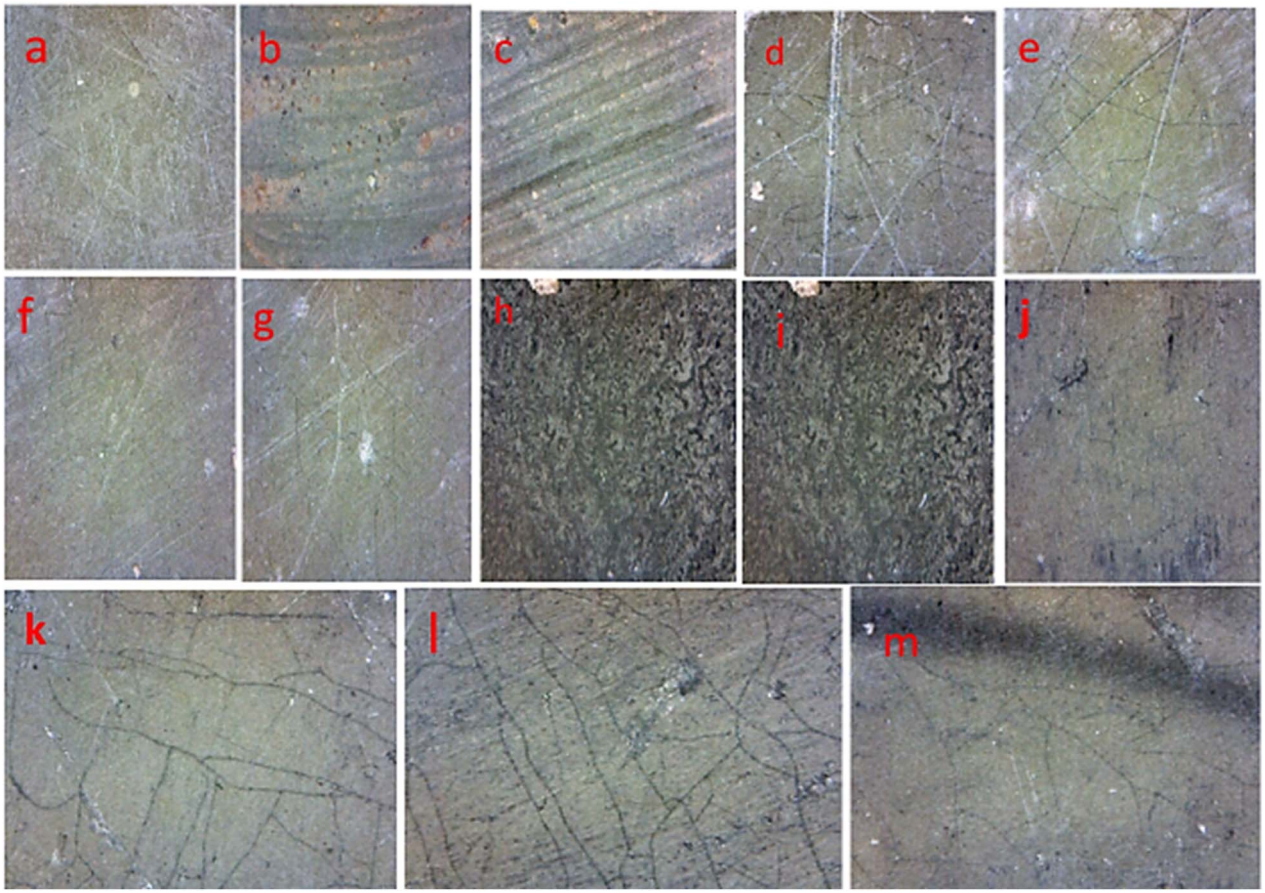

Fig. 7 Samples before and after cleaning of the tintype photo from dust: (a) control sample, (b) solid control, (c) swab, (d) gel agarose, (e) gel agarose + ZnO, (f) gel agarose + carbon dots, and (g) gel agarose + graphitic carbon nitrate and from soot: (h) solid control, (i) swab, (j) gel agarose, (k) gel agarose + ZnO, (l) gel agarose + carbon dots, and (m) gel agarose + graphitic carbon nitride.

a more interconnected nanostructure–agarose network and confirms that the dots are not just physically trapped but are chemically integrated within the gel matrix.[80–83]

3.4. Assessment methods for the efficiency of cleaning

3.4.1. Portable digital microscope. A portable digital microscope was employed to examine surface changes of the samples before and after cleaning with the traditional method (*i.e.*, swab), and with agarose gel and agarose gel with ZnO, carbon dots, graphitic carbon nitride, and the efficiency of these treatments in preserving the surface from UV-induced ageing was also assessed. Fig. 7 shows the surface of tintype photograph samples before and after cleaning treatments aimed at removing dust and soot respectively (a) untreated control; (b) solid control (dust); (c) cleaned with swab; (d) agarose gel only; (e) agarose gel with ZnO nanoparticles; (f) agarose gel with carbon dots; (g) agarose gel with graphitic carbon nitrate; (h) solid control (soot); (i) swab-cleaned soot sample; (j) agarose gel on soot; (k) agarose gel + ZnO on soot; (l) agarose gel + carbon dots on soot; and (m) agarose gel + graphitic carbon nitrate on soot. These findings indicate that nanomaterial-supported agarose gels exhibit superior cleaning performance compared with traditional swabbing, providing effective impurity removal while minimizing mechanical damage.[84] The use of agarose-based gels for controlled cleaning is widely adopted in conservation science,[85] and the incorporation of nanoparticles such as ZnO and carbon-based nanostructures has been reported to enhance both cleaning efficiency and antimicrobial activity.[86–88]

To evaluate the performance of various cleaning agents in preserving tintype photographs exposed to environmental dust, multiple gel formulations were tested. Fig. 8 shows microscopic images of the photo surfaces after ageing. Unexpectedly, untreated control samples Fig. 8a and b showed notable particulate accumulation and surface degradation after ageing. Traditional swab cleaning for dust (Fig. 8c) and soot (Fig. 8i) was of limited effectiveness and risked mechanical abrasion. Among gel-based treatments, agarose gel for cleaning dust (Fig. 8d) and soot (Fig. 8j) improved surface clarity; however, the addition of nanomaterials yielded far more acceptable results. Agarose gel containing ZnO nanoparticles for cleaning dust (Fig. 8e) and soot (Fig. 8k) contaminated samples effectively minimized surface residues, consistent with the reported photocatalytic and antimicrobial properties of ZnO. Carbon dots Fig. 8f for dust,[89] Fig. 8l for soot and graphitic carbon nitride Fig. 8g for dust, Fig. 8m for soot also enhanced the cleaning process, likely due to their high surface area and photochemical stability.[90,91]

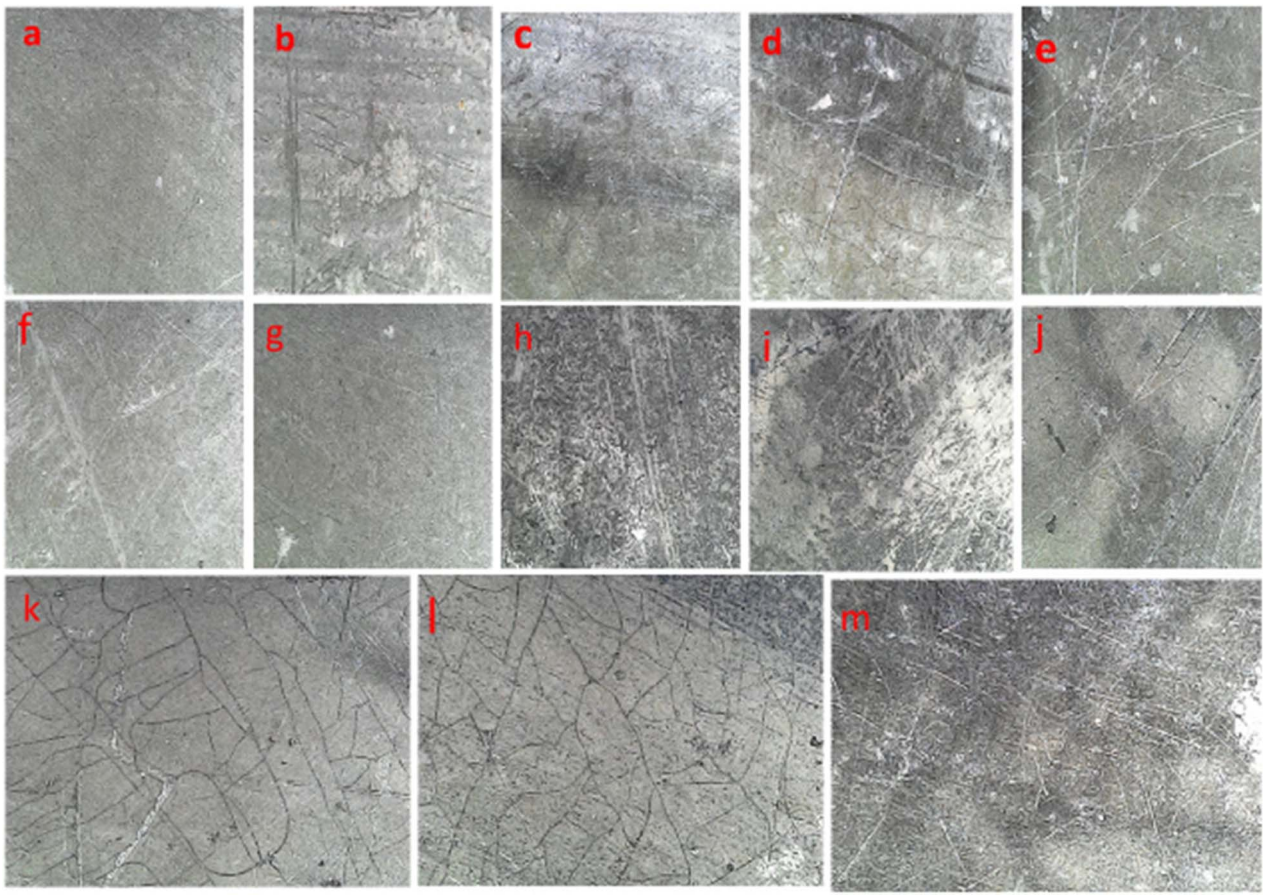

Fig. 8 Samples before and after ageing of tintype photo from dust: (a) control sample, (b) solid control (dust), (c) swab, (d) gel agarose, (e) gel agarose + ZnO, (f) gel agarose + carbon dots, and (g) gel agarose + graphitic carbon nitrate and from soot: (h) solid control (soot), (i) swab, (j) gel agarose, (k) gel agarose + ZnO, (l) gel agarose + carbon dots, and (m) gel agarose + graphitic carbon nitride.

These findings suggest that nanocomposite gels provide a promising, non-invasive alternative for cultural heritage conservation, reducing physical damage while efficiently cleaning delicate surfaces.

3.4.2. Colorimetric measurements. Measuring the degree of color change is of great importance in the field of archaeological materials conservation,[92] especially for tintype photographs, as they are complex materials and highly sensitive to external agents.[93,94] Therefore, when using cleaning and protection materials for this type of photographic image, this factor must be taken into consideration. Based on the data presented in Table 2, two main categories were examined: soot-contaminated samples and dust-contaminated samples. Each category was evaluated before and after cleaning, as well as before and after ageing. The parameters measured are L^*, a^*, b^*, and ΔE^*. For soot samples after cleaning, the control (C) showed L^* 48.30, a^* 0.85, and b^* 7.62, and the solid control sample (S.C) showed L^* 29.20, a^* 1.06, and b^* 4.40. Several cleaning methods were tested, including swabbing, agarose gel, and agarose gel combined with different additives (ZnO, carbon dots, and graphitic carbon nitride). The ΔE values varied considerably. For example, S.C presented a high ΔE of 16.71, swabbing resulted in $\Delta E = 14.46$, agarose gel yielded $\Delta E = 11.34$, and agarose gel + g-C_3N_4 recorded a relatively high ΔE of 13.70. In contrast, agarose gel + ZnO produced the lowest value ($\Delta E = 5.84$), followed by agarose gel + carbon dots ($\Delta E = 7.73$).

For dust samples after cleaning, S.C showed a ΔE of 7.70. Swabbing resulted in $\Delta E = 6.50$, agarose gel gave $\Delta E = 6.80$, agarose gel + ZnO resulted in $\Delta E = 3.35$, agarose gel + carbon dots had $\Delta E = 2.70$, and agarose gel + g-C_3N_4 yielded $\Delta E = 3.09$. To further assess the effectiveness of the cleaning materials in protecting the photographic surface, ultraviolet ageing was performed. For soot samples after ageing, the control (C) showed L^* 44.47, a^* −1.36, and b^* 11.66. The solid control exhibited a high ΔE of 12.83, whereas swabbing showed $\Delta E = 8.64$ and agarose gel resulted in $\Delta E = 8.55$. The lowest values were observed for agarose gel + ZnO ($\Delta E = 2.93$) and agarose gel + carbon dots ($\Delta E = 2.21$). Conversely, agarose gel + g-C_3N_4 had a much higher ΔE of 10.43. These results indicate that some cleaning materials contribute to better long-term color stability. For dust samples after ageing, the solid control displayed a ΔE of 9.30, while the swab-cleaned sample showed $\Delta E = 3.03$. Agarose gel resulted in $\Delta E = 4.45$, agarose gel + ZnO gave $\Delta E = 2.70$, agarose gel + carbon dots recorded $\Delta E = 3.06$, and agarose gel + g-C_3N_4 produced $\Delta E = 2.66$. These findings similarly suggest that the cleaning materials used—particularly agarose

Table 2 Color changes of the tintype photograph

Sample	L^*	a^*	b^*	ΔE^*
Soot before and after cleaning				
C	48.30	0.85	7.62	
S.C	29.20	1.06	4.40	16.71
Swab	32.06	1.11	5.08	14.46
Agarose gel	35.86	1.36	6.34	11.34
Agarose gel + ZnO	42.41	1.76	9.26	5.84
Agarose gel + carbon dots	40.23	1.90	8.99	7.73
Agarose gel + graphitic carbon nitrate	33.00	1.18	5.10	13.7
Dust before and after cleaning				
S.C	41.55	4.12	7.12	7.7
Swab	41.60	1.90	7.75	6.5
Agarose gel	41.18	1.62	8.36	6.8
Agarose gel + ZnO	46.01	2.69	8.59	3.35
Agarose gel + carbon dots	46.62	1.94	10.17	2.7
Agarose gel + graphitic carbon nitrate	46.16	1.86	10.37	3.09
Soot before and after ageing				
C	44.47	−1.36	11.66	
S.C	30.49	−2.57	5.65	12.83
Swab	35.47	−2.50	7.47	8.64
Agarose gel	35.63	−2.53	7.41	8.55
Agarose gel + ZnO	41.43	−1.95	10.26	2.93
Agarose gel + carbon dots	42.12	−1.44	11.02	2.21
Agarose gel + graphitic carbon nitrate	33.67	−2.51	5.98	10.43
Dust before and after ageing				
S.C	53.52	−0.55	8.59	9.30
Swab	41.61	−1.96	9.54	3.03
Agarose gel	40.02	−2.06	9.43	4.45
Agarose gel + ZnO	47.34	−1.22	11.80	2.7
Agarose gel + carbon dots	47.23	−2.25	11.60	3.06
Agarose gel + graphitic carbon nitrate	47.01	−2.22	11.85	2.66

gel with nanomaterial additives—help maintain color stability over time. The authors conclude that agarose gel + ZnO (ΔE = 5.84) and agarose gel + carbon dots (ΔE = 7.73) are highly efficient in cleaning soot stains from the photograph surface without causing noticeable alteration to the color of the original image. For dust stains, agarose gel + ZnO (ΔE = 3.35), agarose gel + carbon dots (ΔE = 2.70), and agarose gel + graphitic carbon nitride (ΔE = 3.09) also proved to be highly effective, achieving cleaning without inducing significant color change.

Following UV ageing, the soot-cleaned samples treated with agarose gel + ZnO (ΔE = 2.93) and agarose gel + carbon dots (ΔE = 2.21) demonstrated superior performance in protecting the photographic surface from ageing effects. Similarly, for dust-cleaned samples, agarose gel + ZnO (ΔE = 2.70), agarose gel + carbon dots (ΔE = 3.06), and agarose gel + graphitic carbon nitride (ΔE = 2.66) showed clear advantages in maintaining color stability and enhancing resistance to ageing.

3.4.3. Attenuated total reflectance-Fourier transform infrared (ATR-FTIR) spectroscopy. The results of the infrared analysis are divided into two main sections. The first section examines the effectiveness of several cleaning methods, including traditional swab cleaning and alternative cleaning methods using agarose gel and agarose gels incorporated with nanomaterials such as zinc oxide, carbon dots, and graphitic carbon nitride, in removing dust and soot stains from the surface of the tintype image. The second section focuses on evaluating the effectiveness of these cleaning methods in shielding the surface of the tintype image from UV ageing. In the first section, FTIR spectroscopy was employed to assess the chemical efficiency of the various cleaning methods by comparing the spectral responses of treated samples with those of the untreated dusted control sample. The ATR-FTIR spectra of the blank (control) sample revealed characteristic functional groups of the collodion layer, including C–H_2 stretching vibrations (2800–3000 cm^{-1}), C=O stretching (1650–1800 cm^{-1}), C–O–C ether linkage (1000–1200 cm^{-1}), and C–N vibrations (600–1000 cm^{-1}).[11,95–98] In contrast, the ATR-FTIR spectra of untreated dusted samples exhibited the presence of O–H stretching vibrations at 3675 cm^{-1}, along with strong Si–O peaks in the 1100–1000 cm^{-1} region attributed to silicates (1027 cm^{-1}).[99] Characteristic carbonate bands appeared at 1150–1100 cm^{-1} and 600–650 cm^{-1} (1116 cm^{-1} and 692 cm^{-1}). Lower-frequency regions below 800 cm^{-1} indicated the presence of metal oxides and aluminosilicate minerals (788 cm^{-1} and 692 cm^{-1}), reflecting the mixed organic–inorganic composition of dust.[100] Notably, the distinctive collodion peaks disappeared in the solid control (*i.e.*, the untreated dusted sample), indicating that the surface was entirely covered by dust deposits. A comparative analysis between the dusted sample and the sample cleaned using a swab revealed the reappearance of characteristic collodion peaks, including C–H_2 bands at 2854 and 2929 cm^{-1}, a C=O peak at 1693 cm^{-1}, C–O–C at 1031 cm^{-1}, and C–N at 700 cm^{-1}. Additionally, a noticeable reduction was observed in the O–H peak at 3625 cm^{-1}, the Si–O peak at 916 cm^{-1}, and the carbonate peak at 794 cm^{-1}. These findings suggest that the sample has undergone a cleaning process; however, it is evident that residual contaminants remain on the surface. The sample cleaned with agarose gel exhibited a reduction in the absorbance of contaminant-related peaks, with some peaks disappearing entirely. The O–H group appeared at 3621 cm^{-1}, and the Si–O peak was observed at 1026 cm^{-1}. Meanwhile, the characteristic collodion peaks, including C–H stretching at 2856 and 2927 cm^{-1}, C=O at 1693 cm^{-1}, and C–O–C at 1031 cm^{-1}, remained clearly visible, indicating significantly fewer residual contaminants compared to the swab-cleaned samples. Enhanced cleaning performance was observed in the sample cleaned with agarose gel containing ZnO nanoparticles. In this sample, the O–H peak decreased further to 3620 cm^{-1}, and the Si–O peak shifted to 912 cm^{-1}. At the same time, the characteristic collodion peaks were clearly restored, including C–H_2 bands at 2860 and 2933 cm^{-1}, C=O at 1691 cm^{-1}, C–O–C at 1031 cm^{-1}, and C–N at 796 cm^{-1}. Along with the full appearance and intensification of the distinctive collodion peaks, one also observes that the characteristic dust peaks vanish in the samples that were cleaned using both agarose with carbon dots and agarose with graphitic carbon nitride, as shown in Fig. 9.

For soot-contaminated samples, the ATR-FTIR spectra of the untreated soot samples (solid control sample) revealed the presence of several distinctive soot function groups, such as C–O–C at 1029 cm^{-1}, and O–H at 798 cm^{-1}.[101] The swab-cleaned

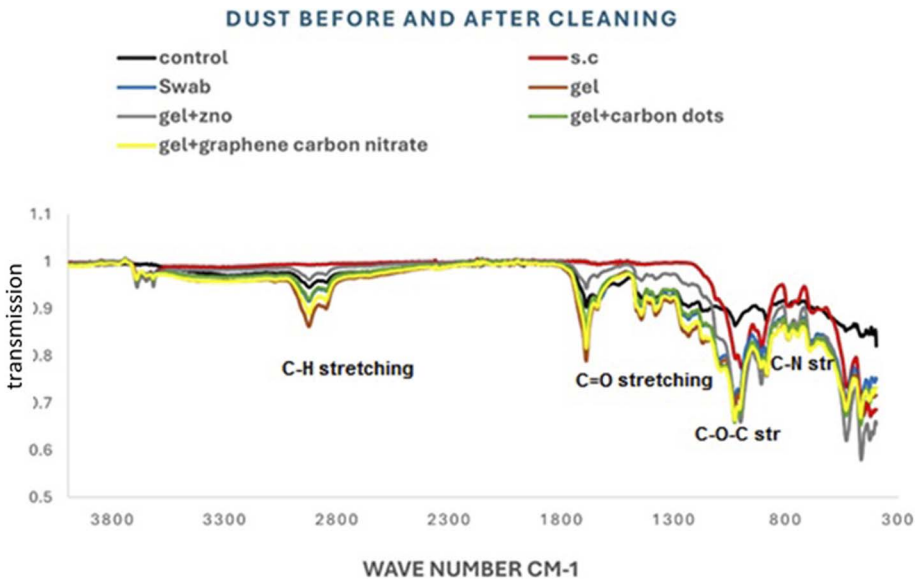

Fig. 9 FTIR data for the samples before and after cleaning dust stains.

sample revealed the presence of functional groups that are typical of soot, namely C–O–C at 1031 cm^{-1} and O–H at 788 cm^{-1}, with slight shifts in the wavenumbers of both bands indicating partial reduction but not complete removal. In the sample cleaned with agarose gel, the C–O–C soot peak at 1029 cm^{-1} disappeared, while the O–H peak shifted to 792 cm^{-1}, confirming a reduction compared to the solid control sample (798 cm^{-1}). Additionally, the emergence of collodion peaks is noted: C–H_2 at 2929 cm^{-1} and 2856 cm^{-1}, C═O at 1693 cm^{-1}, C–O–C at 1029 cm^{-1}, and C–N at 887 cm^{-1}. This indicates partial but incomplete cleaning. The samples cleaned with agarose gel containing ZnO, carbon dots, or graphitic carbon nitride exhibited elimination of soot-related peaks and the emergence of collodion peaks, thereby validating the efficacy of the cleaning process. The following functional groups were detected during the cleaning process for zinc oxide, carbon dots, and graphite carbon nitrite, respectively: C–H_2 at (2931, 2856 cm^{-1}), (2925, 2858 cm^{-1}), and (2927, 2852 cm^{-1}); C═O at 1691 cm^{-1}, 1693 cm^{-1}, and 1693 cm^{-1}; C–O–C at 1031 cm^{-1},

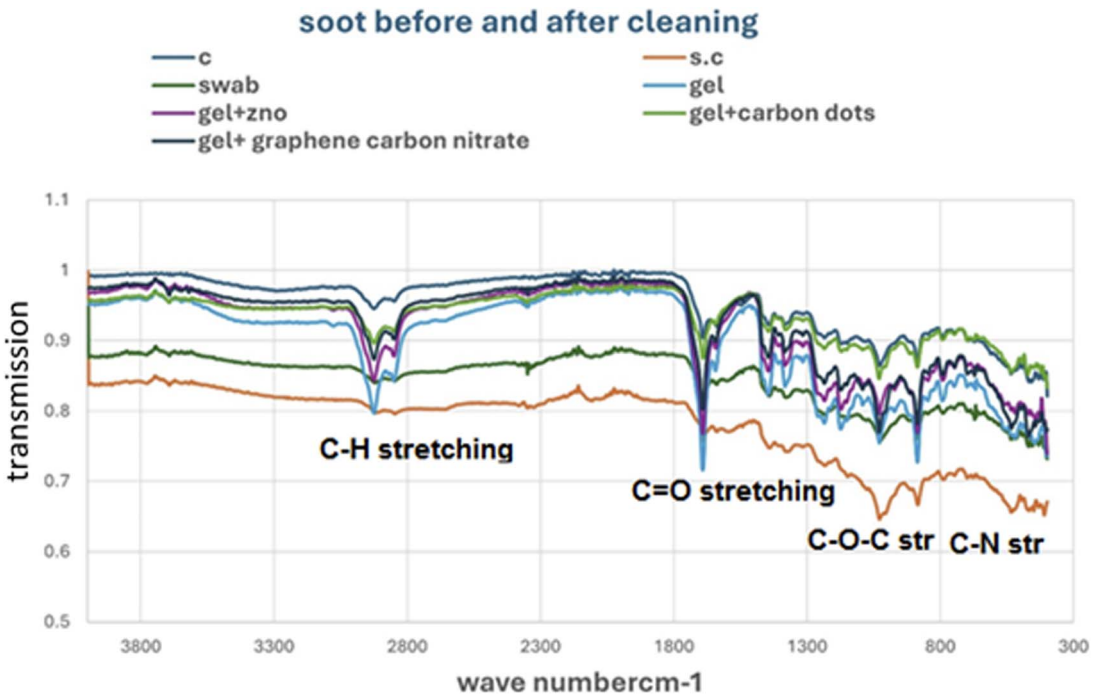

Fig. 10 FTIR data for the samples before and after cleaning soot stains.

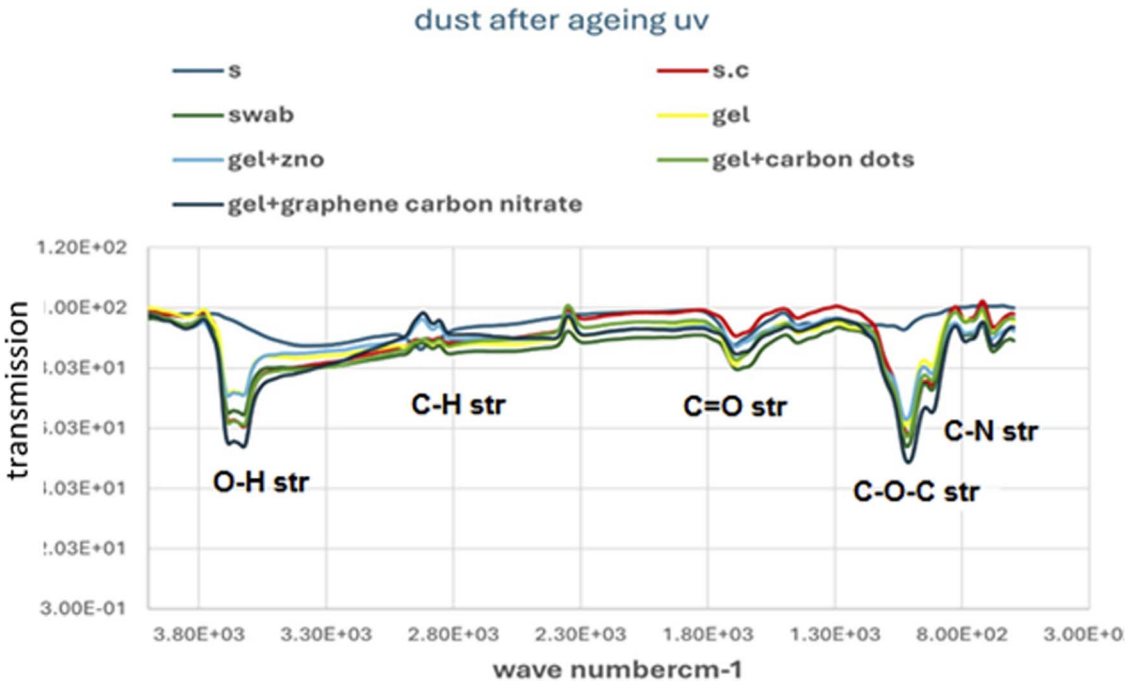

Fig. 11 FTIR data for the dust cleaning samples after UV ageing.

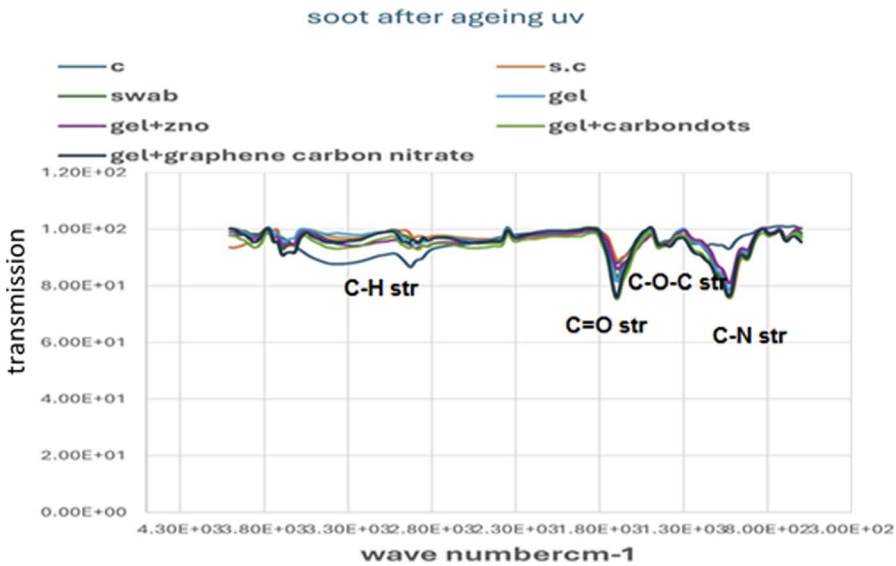

Fig. 12 FTIR data for the soot cleaning samples after UV ageing.

1031 cm^{-1}, and 1031 cm^{-1}; and C–N at 888 cm^{-1}, 889 cm^{-1}, and 889 cm^{-1} (Fig. 10).

The protective efficacy of cleaning materials against UV ageing was then assessed. Samples treated with swabs exhibited a marginal elevation in the peak of the C═O group at 1706 cm^{-1}; thereby corroborating surface oxidation attributed to dust residues present on the surface. The samples cleaned with agarose and those supplemented with nanometric materials demonstrated no chemical alterations due to photoageing, thereby affirming the efficacy of these materials in cleaning and safeguarding the surface from chemical damage induced by photochemical reactions (Fig. 11). The ageing analysis of the purified samples (soot) indicated that the sample treated with a swab exhibited an increase in the intensity of the C═O bond,

confirming the occurrence of oxidation. Similarly, the ageing analysis of soot-cleaned samples showed an increase in the C=O bond intensity in swab-treated samples, confirming the occurrence of oxidation. In contrast, no chemical alterations were observed in samples cleaned with agarose gel or nanocomposite agarose systems, further confirming their superior protective performance (Fig. 12).

4. Conclusions

This research confirms that for the conservation of tintype photographs, it is imperative to employ cleaning methods that are adapted to the complex multi-layering of such images as well as their high susceptibility to environmental/mechanical factors. It is shown that the classical method of mechanical swabbing is ineffective for removing particulate contaminations and accelerates the degradation of the image surface after ageing. Meanwhile, nanomaterial-based agar gels with complexes of ZnO nanoparticles and carbon dots were found to effectively remove dust and soot from tintype surfaces without adversely affecting their chemical, physical, or optical properties. The small change in color tone and integrity of the image surface after simulated ageing with UV radiation testified to the effectiveness of nanomaterial-based cleaning gels for the conservation of tintype images. Based on these positive outcomes, it should be noted that the present approach is intended for the removal of surface contaminants and for preventive conservation purposes. Chemically bound corrosion products, such as silver sulfide formed by long-term exposure to sulfur-containing pollutants, were not specifically targeted in this study. It is important that future studies continue to explore the application of nanocomposite agarose gels through long-term ageing tests under various environmental conditions, such as variations of temperature, humidity, and lighting. Moreover, research is needed to establish optimized gel formulations, study other nanomaterials, and assess controlled concentration factors to improve cleaning efficiency and achieve full compatibility with historical photographic materials. This work should be expanded to other nineteenth-century photographic processes so that it may contribute to the development of standardized, safe, and sustainable nanotechnology-based cleaning methods for the preservation of our photographic heritage.

Author contributions

Hadeer Mamdouh Ahmed ELdeeb contributed to data curation, investigation, resources, and writing – review and editing. Mona Fouad Ali was responsible for supervision, investigation, and writing – review and editing. Maha Ahmed Ali participated in supervision, investigation, resources, and writing – review, editing. Nasser Badawy Morgan was involved in methodology, supervision, investigation, and writing – review and editing. Ahmed Nabile Emam contributed significantly to the preparation and complete characterization of nanomaterials used in the current investigation, data analysis and curation, investigation, and writing – review and editing of the manuscript. Hadeer Mamdouh Ahmed ElDeeb and Ahmed Nabile Emam contributed equally to this work and share first authorship; both are corresponding authors.

Conflicts of interest

There are no conflicts to declare.

Data availability

All data generated or analyzed during this study are included in this published article.

Supplementary information (SI) is available. See DOI: https://doi.org/10.1039/d6ra00164e.

Notes and references

1 O. Enwezor, *Archive Fever: Uses of the document in contemporary art*, 2008, vol. 1, pp. 11–51.
2 C. Caraffa, *Collection and Curation*, 2018, **37**, 146–150.
3 C. Riggs, *Mus. Hist. J.*, 2017, **10**, 140–161.
4 J. Roberts, *Photography and its violations*, Columbia University Press, 2014.
5 E. S. Cooper, *Etched with Light: a Survey History of Photography in the Territory of Arizona*, Arizona State University, 1993, pp. 1856–1880.
6 J. G. Schimmelman, in *Tintype in America*, The American Philosophical Society Press, 2007.
7 C. Pfeiffer, *A Descriptive Analysis of Ten Painted Tintypes from the George Eastman House Collection*, PhD thesis, Toronto Metropolitan University, 2012.
8 C. E. Rogge and K. Lough, *Journal of the American Institute for Conservation*, 2016, **55**, 138–147.
9 E. N. El Shamy, Rehousing a historical tintype photographs by designing a new preserving photographic album, *Majallat Kulliyat Al-Āthār*, Cairo University, 2019, vol. 6, pp. 39–48.
10 Z. Berger Haladová, R. Bohdal, Z. Černeková, P. Štancelová, A. Ferko, J. Blaško Križanová, J. Hojstričová and K. Baráthová, *Sensors*, 2023, **23**, 2303.
11 G. Mauran, Rock paintings and microorganisms: a new insight on Escoural Cave, MSc thesis, Universidade de Évora, Portugal, 2016.
12 B. Lavédrine and J.-P. Gandolfo, *Photographs of the Past: Process and Preservation*, Getty Publications, 2009.
13 P. W. Baas, M. M. Black and G. A. Banker, *J. Cell Biol.*, 1989, **109**, 3085–3094.
14 M. J. Lourenço and J. P. Sampaio, *Int. Biodeterior. Biodegrad.*, 2009, **63**, 496–502.
15 M. E. Osman, S. Ismael, E. Ciliberto, S. Stefani and Y. M. Elsaba, *Int. J. Conserv. Sci.*, 2022, **13**, 527–540.
16 H. M. A. Eldeeb, M. F. Ali, M. M. Mansour, M. A. A. Ahmed and M. Z. Salem, *Microb. Pathog.*, 2022, **169**, 105632.
17 E. B. Reijers, *How to Preserve Photographic Artworks for the Future: Chemical and Physical Interactions and Implications for Conservation Strategies*, PhD thesis, Utrecht University, 2017.

18 C. Cabello Briones, S. Mayorga Pinilla, D. Vázquez Moliní and A. Álvarez Fernández-Balbuena, *Heritage Sci.*, 2021, **9**, 1–12.
19 M. I. Jamil, X. Zhan, F. Chen, D. Cheng and Q. Zhang, *ACS Appl. Mater. Interfaces*, 2019, **11**, 31532–31542.
20 A. Arana, M. Dolores Rodriguez Laso, M. Ángeles Olazábal and M. Pérez-Alonso, *Stud. Conserv.*, 2004, **49**, 215–244.
21 M. Abdel-Hamied, H. M. Hassan, Y. A. Mohamed, M. E. M. Ismail, Y. Farid, H. Mohamed, S. H. Ismail, M. Z. M. Salem and R. R. A. Hassan, *Heritage Sci.*, 2024, **12**, 104.
22 B. A. Campbell and C. Baars, *The Curation and Care of Museum Collections*, Routledge, New York, 2019.
23 M. Shelley, *The Care and Handling of Art Objects: Practices in the Metropolitan Museum of Art (Revised Edition, 2019)*, Metropolitan Museum of Art, 2019.
24 M. V. C. Lozano, G. Sciutto, S. Prati and R. Mazzeo, *Heritage Sci.*, 2022, **10**, 114.
25 M. H. Ellis, *The Care of Prints and Drawings*, Rowman & Littlefield, 2016.
26 C. L. Scott, *AIC Objects Specialty Group Postprints*, 2012, vol. 19, pp. 71–83.
27 M. Ali, *Egypt. J. Archeol. Restor. Stud.*, 2022, **12**, 7–27.
28 D. Chan, *Development of an Inkjet Printing System on a Flatbed Router*, University of Waterloo, 2010.
29 Q. Xu, W. Li, L. Ding, W. Yang, H. Xiao and W.-J. Ong, *Nanoscale*, 2019, **11**, 1475–1504.
30 M. Zhang, J. Zhao, S. Wang, Z. Dai, S. Qin, S. Mei, W. Zhang and R. Guo, *J. Colloid Interface Sci.*, 2025, **678**, 593–601.
31 L. O. Cinteză and M. A. Tănase, in *Thin films*, IntechOpen, 2020.
32 S. Mandal, P. Kumar, B. Satpathy, K. Das and S. Das, *J. Cult. Herit.*, 2024, **69**, 94–112.
33 A. Helal, A. E. M. Fouda and S. Shaarawy, *Egypt. J. Chem.*, 2024, **67**, 121–140.
34 M. Busila, V. Musat, P. Alexandru, C. Romanitan, O. Brincoveanu, V. Tucureanu, I. Mihalache, A.-V. Iancu and V. Dediu, *Int. J. Mol. Sci.*, 2023, **24**, 16939.
35 L. Xin, 2022.
36 M. Doni, I. Fierascu and R. C. Fierascu, *Appl. Sci.*, 2024, **14**, 11363.
37 D. Bhanderi, P. Lakhani and C. K. Modi, *RSC Sustainability*, 2024, **2**, 265–287.
38 L. Sun, T. Du, C. Hu, J. Chen, J. Lu, Z. Lu and H. Han, *ACS Sustain. Chem. Eng.*, 2017, **5**, 8693–8701.
39 H. He, X. Wang, Z. Feng, T. Cheng, X. Sun, Y. Sun, Y. Xia, S. Wang, J. Wang and X. Zhang, *J. Mater. Chem. B*, 2015, **3**, 4786–4789.
40 A. Emam, S. A. Loutfy, A. A. Mostafa, H. Awad and M. B. Mohamed, *RSC Adv.*, 2017, **7**, 23502–23514.
41 B. Bekele, L. Jule and A. Saka, *Digest J. Nanomater. Biostruct.*, 2021, **16**, 471–478.
42 Y.-Q. Li, S.-Y. Fu and Y.-W. Mai, *Polymer*, 2006, **47**, 2127–2132.
43 S. El-Shahat, A. N. Emam, M. I. El-Dessouky and G. G. Mohamed, *Egypt. J. Chem.*, 2025, **68**, 103–131.
44 M. Waheed, A. N. Emam and G. G. Mohamed, *Egypt. J. Chem.*, 2025, **68**, 431–450.
45 A. N. Emam, L. Osama, H. H. Beherei and M. Mabrouk, *Mater. Adv.*, 2026, **7**, 1138–1152.
46 T. Wang, B. Song and L. Wang, *Polymers*, 2020, **12**, 76.
47 M. Taha, A. Khalid, M. G. Elmahgary, S. S. Medany and Y. A. Attia, *Sci. Rep.*, 2024, **14**, 4184.
48 A. Emam, A. Mostafa, M. Mohamed, A.-S. Gadallah and M. El-Kemary, *J. Lumin.*, 2018, **200**, 287–297.
49 S. Cao, J. Low, J. Yu and M. Jaroniec, *Adv. Mater.*, 2015, **27**, 2150–2176.
50 T. Ahmed and T. Edvinsson, *J. Phys. Chem. C*, 2020, **124**, 6395–6404.
51 U. Manzoor, M. Islam, L. Tabassam and S. U. Rahman, *Phys. E*, 2009, **41**, 1669–1672.
52 R. Thangavel, M. Rajagopalan and J. Kumar, *Solid State Commun.*, 2006, **137**, 507–511.
53 C.-L. Dong, J. Guo, Y.-Y. Chen and C.-L. Chang, *SPIE Newsroom*, 2007, **3**, 3–6.
54 K. S. Babu, A. R. Reddy, C. Sujatha and K. V. Reddy, *Mater. Lett.*, 2013, **99**, 97–100.
55 N. Kamarulzaman, M. F. Kasim and R. Rusdi, *Nanoscale Res. Lett.*, 2015, **10**, 1034.
56 A. K. Jaimes, V. Ayala-Peña, A. Buzzi, V. Álvarez and V. Lassalle, *Viruses*, 2026, **18**(1), 76.
57 J. Ren, F. Weber, F. Weigert, Y. Wang, S. Choudhury, J. Xiao, I. Lauermann, U. Resch-Genger, A. Bande and T. Petit, *Nanoscale*, 2019, **11**, 2056–2064.
58 H. Ding, X.-H. Li, X.-B. Chen, J.-S. Wei, X.-B. Li and H.-M. Xiong, *J. Appl. Phys.*, 2020, **127**(23), 231101.
59 B. Li, T. Tian, Y. Zheng, D. Jiang, G. Xu, Y. Sun, Z. Li and Y. Yuan, *Chem.–Eur. J.*, 2025, **31**, e202500297.
60 X. Li, J. Bai, J. Li, C. Li, X. Zhong and S. Deng, *RSC Adv.*, 2020, **10**, 7019–7025.
61 H. B. A. Sousa, C. S. M. Martins and J. A. V. Prior, *Nanomater.*, 2021, **11**, 611.
62 H.-L. Yang, L.-F. Bai, Z.-R. Geng, H. Chen, L.-T. Xu, Y.-C. Xie, D.-J. Wang, H.-W. Gu and X.-M. Wang, *Mater. Today Adv.*, 2023, **18**, 100376.
63 A. E. Morales, E. S. Mora and U. Pal, *Rev. Mex. Fis.*, 2007, **53**, 18–22.
64 A. Alaghmandfard and K. Ghandi, *Nanomater.*, 2022, **12**(2), 294.
65 G. Yao, Y. Liu, J. Liu and Y. Xu, *Molecules*, 2022, **27**, 1754.
66 J. Z. Kong, H. F. Zhai, W. Zhang, S. S. Wang, X. R. Zhao, M. Li, H. Li, A. D. Li and D. Wu, *Nanoscale Res. Lett.*, 2017, **12**, 526.
67 S. Borthakur, R. Das, P. Basyach, K. Sonowal and L. Saikia, *RSC Adv.*, 2024, **14**, 1156–1168.
68 A. S. Syeda, *A Novel Approach to Sustainable Energy through Modified Sg-C3N4@ Lignin Catalyst for Model Oil Desulfurization*, Doctoral Dissertation, Department of Chemistry COMSATS, University Islamabad Lahore Campus, 2025.
69 Y. Yang, W. Lei, Y. Xu, T. Zhou, M. Xia and Q. Hao, *Microchim. Acta*, 2018, **185**, 39.

70 A. Thomas, A. Fischer, F. Goettmann, M. Antonietti, J.-O. Müller, R. Schlögl and J. M. Carlsson, *J. Mater. Chem.*, 2008, **18**, 4893–4908.
71 S. P. Pattnaik, A. Behera, S. Martha, R. Acharya and K. Parida, *J. Mater. Sci.*, 2019, **54**, 5726–5742.
72 F. Fina, S. K. Callear, G. M. Carins and J. T. Irvine, *Chem. Mater.*, 2015, **27**, 2612–2618.
73 M. Suneel, M. A. Khan, N. Tabassum, A. R. Khan, Z. Feroz and Q. I. Rahman, *Environ. Earth Sci. Proc.*, 2025, **32**, 18.
74 N. Jayarambabu, B. S. Kumari, K. V. Rao and Y. Prabhu, *Int. J. Curr. Eng. Technol.*, 2014, **4**, 3411–3416.
75 P. Shubha, K. Harini, S. Shyamsundar, P. Shubha and S. Shyamsundar, *Cureus*, 2025, **17**(11), e97191.
76 J. Liu, R. Li and B. Yang, *ACS Cent. Sci.*, 2020, **6**, 2179–2195.
77 N. Gogoi, M. Barooah, G. Majumdar and D. Chowdhury, *ACS Appl. Mater. Interfaces*, 2015, **7**, 3058–3067.
78 S. Pourali, R. Amrollahi, S. Alamolhoda and S. Masoudpanah, *Sci. Rep.*, 2025, **15**, 462.
79 H. Jung, V. S. Sapner, A. Adhikari, B. R. Sathe and R. Patel, *Front. Chem.*, 2022, **10**, 881495.
80 N. Ismayilova, M. K. Zia, H. S. Akkaya, S. Ulag, Y. Guldorum, E. T. Oner, E. Ince, L. Duta and O. Gunduz, *Biomimetics*, 2024, **9**, 508.
81 M. H. Suhag, A. Khatun, I. Tateishi, M. Furukawa, H. Katsumata and S. Kaneco, *ACS Omega*, 2023, **8**, 11824–11836.
82 M. H. Suhag, A. Khatun, I. Tateishi, M. Furukawa, H. Katsumata and S. Kaneco, *ACS Omega*, 2023, **8**, 11824–11836.
83 S. M. Jambi, J. Chen, W. Zhang, S. Fu, Y. Zhou, J. B. Domena, N. M. Brejcha, F. Zhang and R. M. Leblanc, *Colloids Surf., A*, 2023, **669**, 131522.
84 P. Baglioni, D. Chelazzi and R. Giorgi, *Nanotechnologies in the Conservation of Cultural Heritage: a Compendium of Materials and Techniques*, Springer, 2014.
85 P. Baglioni, E. Carretti and D. Chelazzi, *Nat. Nanotechnol.*, 2015, **10**, 287–290.
86 N. Khaksar-Baghan, A. Koochakzaei and Y. Hamzavi, *Heritage Sci.*, 2024, **12**, 248.
87 D. Chelazzi and P. Baglioni, *Langmuir*, 2023, **39**, 10744–10755.
88 J. Nan, Y. Chu, R. Guo and P. Chen, *Front. Mater.*, 2024, **11**, 1449614.
89 S. Y. Lim, W. Shen and Z. Gao, *Chem. Soc. Rev.*, 2015, **44**, 362–381.
90 A. Hayat, A. G. Al-Sehemi, K. S. El-Nasser, T. Taha, A. A. Al-Ghamdi, J. A. S. Syed, M. A. Amin, T. Ali, T. Bashir and A. Palamanit, *Int. J. Hydrogen Energy*, 2022, **47**, 5142–5191.
91 Y. Wang, X. Wang and M. Antonietti, *Angew. Chem., Int. Ed.*, 2012, **51**, 68–89.
92 R. El-Gamal, K. El-Nagar, N. A. Tharwat and G. Abdel-Maksoud, *Pigm. Resin Technol.*, 2024, **53**, 94–102.
93 M. Nizette and J. Lyall, *ICCM Bulletin*, 1982, **8**, 9–25.
94 M. Osterman, *The Concise Focal Encyclopedia of Photography*, 2008, pp. 27–157.
95 M. H. McCormick- Goodhart, *Research on Collodian Glass Plate Negatives: Coating Thickness and FTIR Identification of Varnishes*, 1989, pp. 135–152.
96 C.-l. Cai, X. Han, X.-l. Niu and W.-g. Liu, *Def. Technol.*, 2013, **9**, 167–170.
97 M. Oravec, K. Haberová, V. Jančovičová, Z. Machatová, M. Čeppan and C. W. Huck, *Microchem. J.*, 2019, **150**, 104202.
98 J. M. Walker and B. H. Berrie, *J. Cult. Herit.*, 2023, **63**, 1–10.
99 H. M. Eldeeb, M. F. Ali, M. A. Ali, N. A. A. Ghany and N. Morgan, *Discover Appl. Sci.*, 2026, **8**, 283.
100 A. A. Shaltout, M. A. Allam, N. Y. Mostafa and Z. K. Heiba, *Arch. Environ. Contam. Toxicol.*, 2016, **70**, 544–555.
101 R. R. A. Hassan, H. M. Hassan, Y. A. Mohamed, M. E. Ismail, Y. Farid, H. Mohamed, S. H. Ismail, M. Z. Salem and M. Abdel-Hamied, *Heritage Sci.*, 2023, **11**, 1–26.